ESD-TR-91-080

Technical Report
919

Performance of Ground-Based Infrared Detectors for Acquisition of Satellites

D.R. Hearn

13 September 1991

Lincoln Laboratory
MASSACHUSETTS INSTITUTE OF TECHNOLOGY
LEXINGTON, MASSACHUSETTS

Prepared for the Department of the Army
under Air Force Contract F19628-90-C-0002.

This report is based on studies performed at Lincoln Laboratory, a center for research operated by Massachusetts Institute of Technology. The work was sponsored by the Department of the Army under Air Force Contract F19628-90-C-0002.

The ESD Public Affairs Office has reviewed this report, and it is releasable to the National Technical Information Service, where it will be available to the general public, including foreign nationals.

This technical report has been reviewed and is approved for publication.

FOR THE COMMANDER

Hugh L. Southall

Hugh L. Southall, Lt. Col., USAF
Chief, ESD Lincoln Laboratory Project Office

Non-Lincoln Recipients

PLEASE DO NOT RETURN

Permission is given to destroy this document when it is no longer needed.

MASSACHUSETTS INSTITUTE OF TECHNOLOGY
LINCOLN LABORATORY

PERFORMANCE OF GROUND-BASED INFRARED DETECTORS FOR ACQUISITION OF SATELLITES

D.R. HEARN
Group 55

TECHNICAL REPORT 919

13 SEPTEMBER 1991

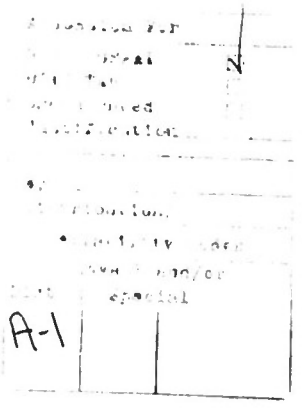

LEXINGTON MASSACHUSETTS

EXECUTIVE SUMMARY

A need exists to be able to detect overflying satellites reliably from the ground, whether for space surveillance, signature studies, or antisatellite systems. Infrared sensors are suggested as a possible means; they are passive and offer much better angular position determination than a microwave radar. Furthermore, an infrared system is much smaller and consumes less power than a radar. Clear weather is required for successful operation, but it may be feasible to place the infrared sensor in an aircraft to fly above cloud cover.

Optical properties of the atmosphere impose limitations on any infrared sensor system for satellite acquisition. The important effects are attenuation of the satellite radiation signal, infrared radiance from the atmosphere itself, and turbulence which blurs the image of the satellite. We have used the LOWTRAN7 code to model the transmission and radiance. Two wavelength bands, 3–5 μm and 8–12 μm, provide windows where the transmission is high enough and radiance low enough for direct observation of satellites. Image spreading by turbulence decreases, but spreading by diffraction increases with increasing wavelength. For a modest-sized (24-inch) telescope, the combined spreading effect is at its minimum around 5 μm in wavelength, depending on the elevation angle.

The range at which a given satellite may be detected varies as the fourth root of the product of the detector quantum efficiency and the number of detecting elements in the array. Only recently have infrared focal-plane arrays become available which have enough detecting elements and detection efficiency to be effective in acquiring most satellites. Large detector arrays can now be obtained for both the 3–5 μm mid-wave and the 8–12 μm long-wave infrared bands. We have evaluated the potential performance of actual arrays based on InSb, HgCdTe, Si:Ga, PtSi, and IrSi detectors.

The performance calculations of this report assume that the infrared sensor array is applied to a reflecting telescope of 60-cm aperture. Uncooled optics are used to relay the satellite image to the focal plane. The relay optics also serve to re-image the primary mirror at the cold aperture stop in the detector dewar. Background radiation from the telescope and its surroundings is thus minimized. We estimate that an optical transmission of 76 percent may be achieved. A cold filter in front of the focal-plane array passes only those wavelengths for which the atmosphere is most transparent. The optical system must include a means to calibrate the responsivities and offsets of the individual detector elements. A flat-field illuminator is easily provided. Detector data are recorded at more than one radiance level, bracketing the level expected during an acquisition search. A set of coefficients derived from the calibration data are applied to correct the real-time detector data.

Immediately prior to an acquisition search, atmospheric background data are recorded digitally. This will require considerable precision, because the background radiance is very large relative to the satellite signals to be detected. The procedure for acquisition is to choose an elevation angle at which the satellite can be detected with confidence, and scan repeatedly across the nominal trajectory of the satellite until it is detected. Each scan is likely to consist of several integration periods, during which the telescope tracks the nominal angular speed of the satellite, separated by rapid steps to the next field of view. During the "staring" period, the frames from the infrared camera are summed to provide the maximum feasible

integration time. This is essential to achieve the best possible signal-to-noise ratio (SNR). If, after subtracting the corresponding background signal, a spot image remains with a net signal over six times the noise level, an object detection is declared and the telescope begins tracking the candidate object.

For each of the candidate sensor arrays the satellite acquisition performance has been calculated, assuming for simplicity that the satellite is in a circular orbit passing overhead. It is assumed that the nominal satellite orbital elements are known, but the present position is uncertain to within a radius of 50 km, perhaps as a result of a recent maneuver. The allowable integration times in such a case depend on where the satellite is at the time of observation. For the typical system parameters used here, they are of order 0.1–1 second. Calculations of transmitted signals and radiant backgrounds assumed midlatitude summer conditions. Rural haze, 23-km visibility, and observations from sea level are assumed. The dominant noise is from the background radiances, both atmospheric and instrumental. However, reported values of minimum-irradiance system electronic noise have been included in the analysis.

The results of the calculations may be seen in two ways. In the first, a nominal satellite size and temperature are chosen, and the zone of range and elevation within which each type of infrared camera can detect the satellite is plotted. We find that the HgCdTe system can detect a 5-m^2, 300-K satellite almost 11,000 km away. The Si:Ga system can detect it at 9,000 km. Of the sensors operating in the 3–5 μm band, InSb performs best, with over 5,000-km detection range. IrSi and PtSi systems can detect at 2,000 and 1,200 km, respectively. These ranges hold for elevations above 45°. Closer to the horizon, increasing atmospheric absorption and radiance cause the detection range to fall off rapidly.

The second type of presentation is a set of contour plots of minimum detectable infrared signature as a function of satellite position. On the plot for each detector, a grid is superimposed to show circular orbits at various altitudes and lines of fixed elevation angle. Given the altitude and signature of a satellite, the range and elevation at which it could be detected by each camera is readily found.

We conclude that all the proposed systems may be used to acquire satellites in low earth orbits. Whether a given detector system will fulfill a particular requirement will depend on the actual altitudes and infrared signatures of the satellites sought. While the present results are very encouraging, we consider it highly desirable to validate these calculations with an actual experimental test. The calculations are based on considerable signal averaging and background subtraction. Noise effects not obeying simple Gaussian statistics, such as turbulent sky radiance fluctuations or "1/f" noise in the detectors, could potentially set more stringent limits to the performance of an infrared satellite acquisition system.

TABLE OF CONTENTS

LIST OF ILLUSTRATIONS

LIST OF TABLES

1. INTRODUCTION

1.1 GROUND-BASED DETECTION OF SATELLITES

The capability to detect overflying satellites from the ground has a number of applications, including space surveillance, signature studies, and antisatellite systems. The means to acquire the satellites include radar and passive electro-optical (E-O) sensors. Microwave radar systems are well developed, but to find a typical satellite at a range of several thousand kilometers they must employ very-high-power transmitters. We have examined the possibility of acquiring satellites from the ground using the infrared sensors currently available. The potential performance of Schottky-barrier infrared sensors for the surveillance application has been studied by Cantella [1]. That report primarily considered open searches for previously unknown objects in space. It is assumed in this study that the elements of the satellite orbit are known approximately, but that the position of the satellite is uncertain to within a specified radius. This report examines the potential performance of several different kinds of infrared sensors in the satellite acquisition role.

1.2 ADVANTAGES OF INFRARED DETECTION

The infrared (IR) sensors we have in mind would be used to passively detect the radiant emissions of the satellite. Unlike radar, a passive sensor system does not advertise its presence and location. This would be a great advantage for a mobile military system; to protect a fleet from observation, for instance. An IR sensor requires a telescope of modest size (~24-inch aperture) to gather radiation from the satellite; the same sensor can provide necessary tracking information after acquisition. The angular precision attained by the IR acquisition system should be much better, of order 10 μrad, as opposed to 1 mrad for a radar acquisition system. A radar system for satellite acquisition, with its associated power supplies, is large and heavy. In contrast, it may be feasible to install an infrared acquisition system in an aircraft, which can fly above the weather (this may be required in some applications, as the IR system requires clear sky to operate).

Given the advantages of passive E-O sensors, the next question is which sensor is best. Visible detectors are simple to use and work very well in the terminator mode (satellite in sunlight, observer in darkness). However, it is desirable to be able to acquire a satellite at any time, day or night. To find a satellite in the earth's shadow, it is necessary to sense its infrared emissions. There are two wavelength ranges in the IR in which the atmosphere is relatively dark and transparent, even in the daytime. They are called midwave infrared (MWIR) (3–5 μm), and long-wave infrared (LWIR) (8–12 μm).

1.3 OBSTACLES TO INFRARED ACQUISITION

Until very recently, imaging IR sensors (sometimes called FLIRs) relied on one or a small number of detectors optically scanned over a scene to produce an image. Such devices are unlikely to be sensitive enough to detect a satellite at the required ranges because the detector dwells for only a short time on any one picture element (pixel). However, several types of staring focal-plane array (FPA) sensors are now available for the IR bands. They include Schottky-barrier photovoltaic arrays on silicon CCDs and

hybrid arrays of InSb, $Hg_{1-x}Cd_xT$-e, or Ga-doped silicon on silicon complementary metal-oxide semiconductor (CMOS) multiplexors. The large number of detectors in these staring arrays make it possible to search a reasonable solid angle with the necessary sensitivity.

The atmosphere not only absorbs IR radiation to some extent at all wavelengths, it also emits IR radiation to a corresponding degree. This is true even in the MWIR and LWIR "windows" mentioned earlier. For some proposed applications, it is necessary to acquire the satellite at the lowest possible elevation angle, where the atmospheric transmission and radiance effects are at their worst. We have attempted to analyze the potential performance of a practical IR acquisition system, using currently available sensors, in relation to actual satellite signatures and known optical properties of the atmosphere.

1.4 PROPOSED EXPERIMENT

An experimental test of IR acquisition of satellites would be highly desirable to verify our performance calculations, make further measurements of satellite signatures, and explore the practical limitations of the present technology. The MIT Lincoln Laboratory Firepond telescope is an ideal testbed for this purpose, as it is already well-equipped to track satellites. It includes an auxiliary telescope of 60-cm aperture, which appears suitable for this purpose. Therefore, the performance calculations in this report are based on the use of that telescope. Comparison with other apertures is very straightforward.

1.5 ORGANIZATION OF REPORT

Sections 2 and 3 of this report outline the characteristics of likely satellites and the relevant properties of the atmosphere. Section 4 describes an IR acquisition system and several different types of detectors which it might use. Section 5 presents an analysis of the performance which may be expected from these detectors based on fundamental physical limitations. For the IR acquisition system, the key result is the maximum range of detection for a given IR signature as a function of satellite elevation angle.

2. SATELLITE CHARACTERISTICS

2.1 INFRARED SIGNATURES

Any object emits electromagnetic radiation by virtue of its thermal energy. The emittance is given by

$$E = \varepsilon \sigma T^4 \quad , \tag{1}$$

where

ε = emissivity of the surface,

σ = the Stefan-Boltzmann constant = 5.67×10^{-8} (W m^{-2} K^{-4})

T = the absolute temperature, in Kelvins (K).

The blackbody radiance within the MWIR (3–5 μm) and LWIR (8–12 μm) wavelength bands is plotted as a function of the temperature of the object addressed in Figure 1. Figure 2 is a plot of the ratio of the radiance in the MWIR band to that in the LWIR band as a function of emitter temperature. Such a plot can be used to estimate a satellite temperature given the measured signatures in the two bands.

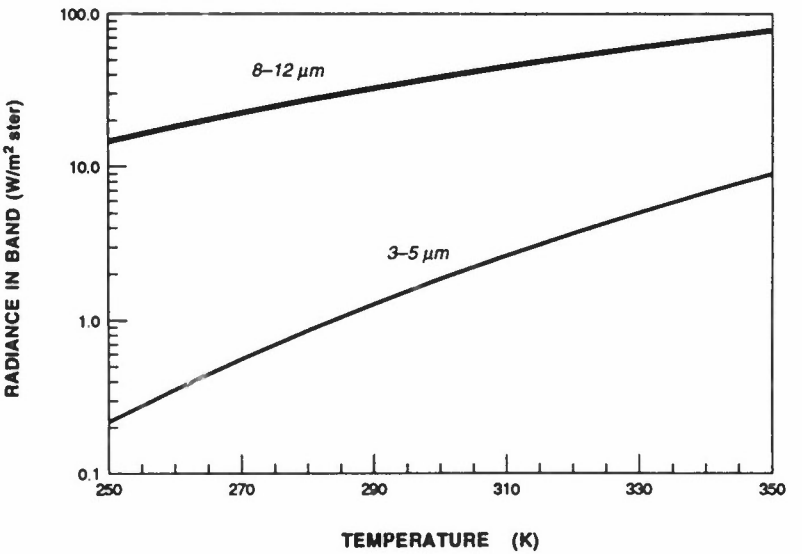

Figure 1. Blackbody radiance within the MWIR (3–5 μm) and LWIR (8–12 μm) spectral bands vs. source temperature.

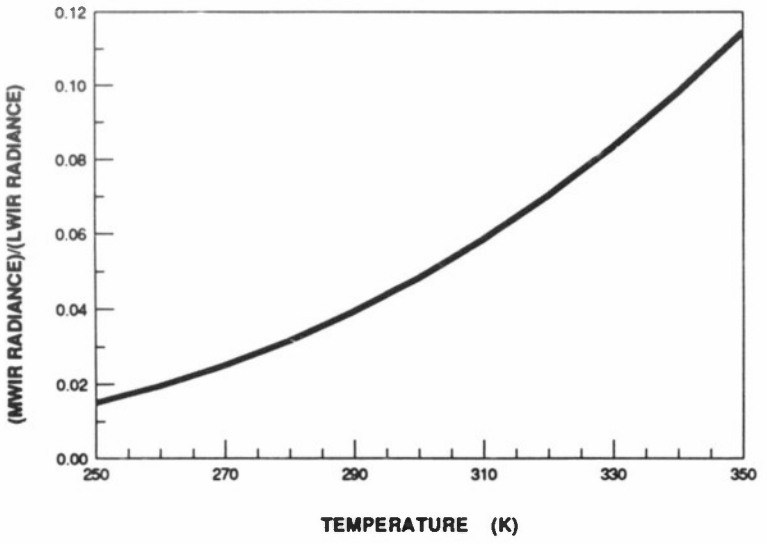

Figure 2. Ratio of blackbody radiance within the MWIR (3–5 μm) band to that in the LWIR (8–12 μm) band vs. source temperature.

In addition to the thermal radiation emitted by a satellite, there is some reflected radiation. Reflected sunlight will especially increase the infrared signature in the 3–5 μm band. The earth will bathe the satellite in thermal radiation with an effective temperature approximately equal to the local ground-level temperature. A fraction of this earth radiation ($1-\varepsilon$, where ε is the satellite emissivity) will be reflected back down toward the observer.

For the satellites of interest in this study, we assume that the projected-area emittance products range from 1–25 m^2. The satellite surface temperatures should be roughly 280–300 K; then the total LWIR (8–12 μm) signatures are in the range 25–1,000 W/ster. Assuming that the emittance is constant over the 3–12 μm wavelength range, the corresponding MWIR (3–5 μm) signatures are roughly 1–50 W/ster.

2.2 TRAJECTORIES

The satellites to be acquired are assumed to be in relatively low earth orbits, (250–2,500-km altitude). The nominal orbital elements of the satellite are assumed to be known; however, a robust acquisition system should be able to acquire a satellite which has just maneuvered to alter its orbit. The

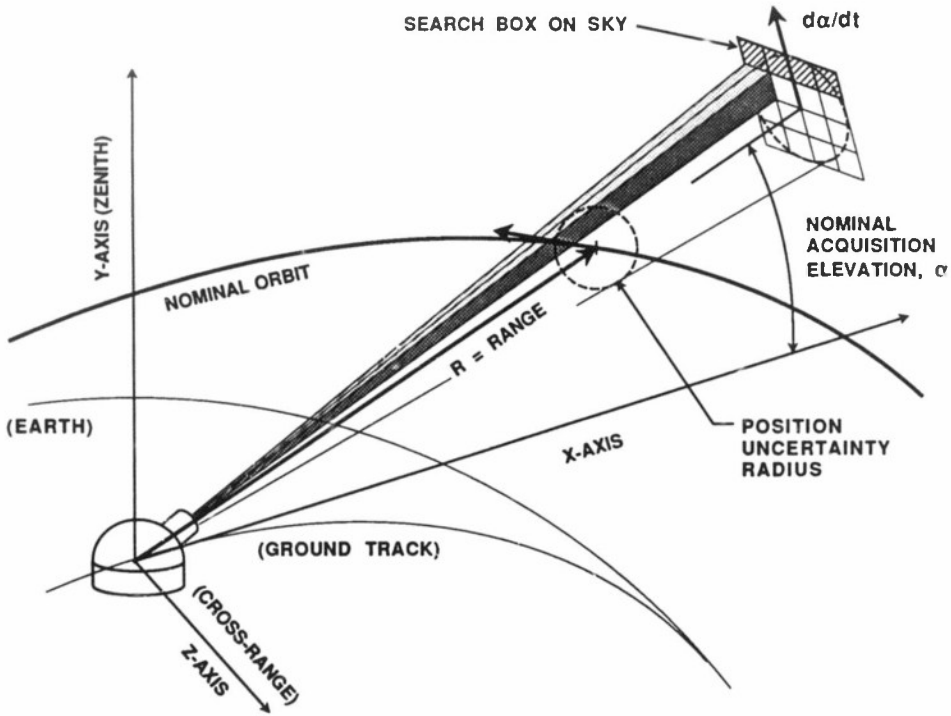

Figure 3. Geometry of acquisition scenario (schematic).

resulting position uncertainty zone may typically be 50 km in radius. To simplify the analysis, it was assumed that the nominal satellite orbit is circular and passes directly over the observer. The relative positions are diagrammed in Figure 3.

For some systems, the satellite must be acquired at the lowest feasible elevation angle. This angle is chosen to ensure a high probability of acquisition as the satellite reaches that elevation. The acquisition telescope is scanned across the position uncertainty zone just rapidly enough to complete the search as the zone rises through the chosen elevation. The orbital velocities of satellites in low earth orbits are roughly 7 km/sec. Their angular speeds as seen from the ground will range between 1 mrad/sec for a

satellite just rising above the horizon to 30 mrad/sec for a very low satellite passing overhead. If acquisition is to take place at elevation angles less than 30° the angular rates will not exceed 5 mrad/sec. Detailed expressions for the angular speeds of satellites are presented in Appendix B.

3. ATMOSPHERIC OPTICS

3.1 RADIANCE AND TRANSMISSION VS. ELEVATION, 3–14 μm

The opacity of the atmosphere in the infrared region is a complicated function of wavelength. It depends on the relative concentration of water vapor and aerosols, which vary with time and place. Fortunately, the problem has been studied extensively, and a computer code, LOWTRAN, has been developed which provides a numerical model of the atmosphere suitable for our analysis [2]. We have obtained the ground-to-space IR transmission and radiance of the atmosphere as a function of wavelength and elevation angle by running LOWTRAN7 on a VAX computer. Conditions assumed for these runs were middle latitude, summer, and rural haze aerosols resulting in 23-km visibility. These conditions are considered representative of the least-favorable season for infrared observations of space. (An IR sensor will perform better in winter, because the lower winter air temperature and water vapor content lead to lower atmospheric opacity.) The transmission is plotted in Figure 4; the radiance is shown in Figure 5. Notice that the wavelengths of greatest transmittance are also those at which the radiance is least, as absorptance and radiance are directly related. At the wavelengths of least transmittance, the radiance resembles that of a blackbody at 295 K. Scattered solar radiation is not included in the plotted radiance, so the curves are most appropriate to nighttime observation. This radiation equals the low-elevation thermal radiance at approximately 3 μm and decreases with increasing wavelength. In daytime, the scattered solar radiation will increase the MWIR background radiation by a fraction, depending on the relative angle of the sun from the look direction.

3.2 TURBULENCE

Turbulence in the atmosphere can also affect observations, increasing the size of the image of a point object which would otherwise be limited by diffraction. (At the ranges of detection anticipated, the satellites would be unresolvable.) We assume that the optics are good enough at these wavelengths to be diffraction-limited. The angular size of the image θ (full width at half-maximum, in radians) is then given by

$$\theta^2 = \left(\frac{1.22\lambda}{D}\right)^2 + \left(\frac{1.22\lambda}{r_0}\right)^2 , \tag{2}$$

where λ is the wavelength, D the diameter of the telescope objective; the atmospheric coherence length is given by [3]

$$r_0 = 0.185\left(\frac{\lambda^2}{\int_0^\infty C_n^2(z)dz}\right)^{3/5} , \tag{3}$$

where C_n^2 is the structure constant of the refractive index fluctuations.

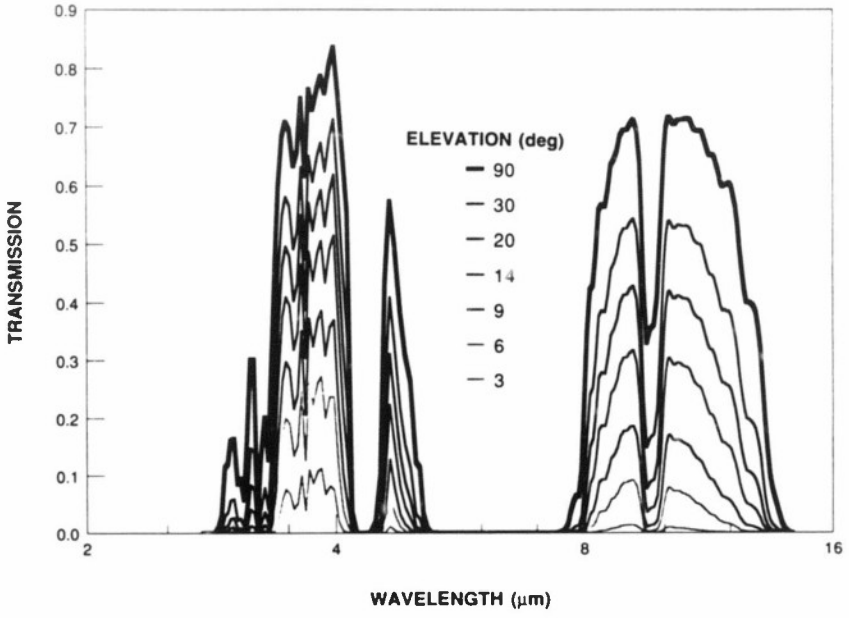

Figure 4. Atmospheric transmissian vs. wavelength for variaus indicated elevatian angles (in degrees). Midlatitude summer conditions with rural aerosol haze giving 23-km visibility have been assumed.

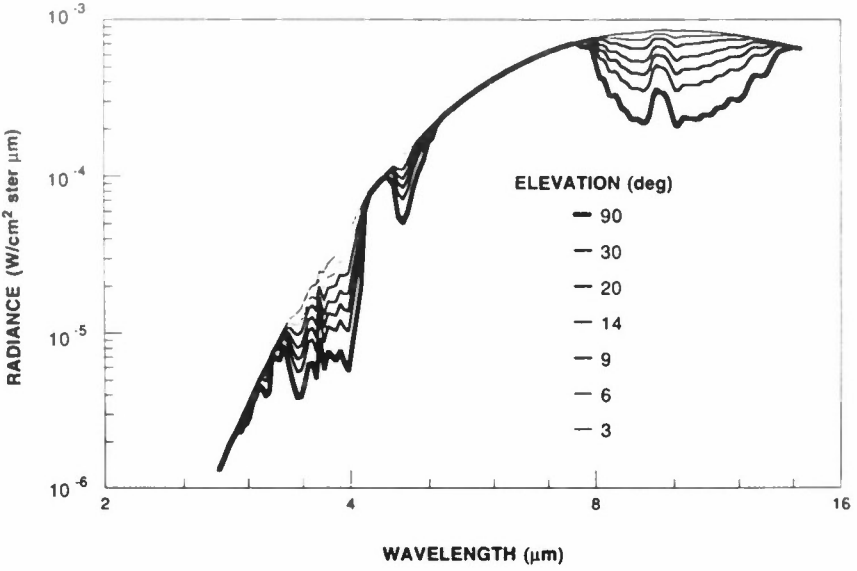

Figure 5. Atmaspheric radiance vs. wavelength for various indicated elevation angles (in degrees). Canditians assumed are the same as for Figure 4. No scattered solar radiation is included.

In Equation (2), the first term is the contribution of diffraction to the image size; the second is caused by turbulence. If we know the coherence length or, alternatively, the size of the atmospheric "seeing disk" for visible light, we need only the wavelength dependence given in Equation (3) to find the value of r_0 for infrared wavelengths. It is then unnecessary to know the structure constant for the whole atmospheric path. It can also be shown from Equation (3) that the dependence of r_0 on the elevation angle, α, is

$$r_0 = r_0\big|_{\alpha=90^\circ} (\sin\alpha)^{3/5} \quad . \tag{4}$$

Typical values of r_0 at high elevations for visible light ($\lambda \approx 0.5$ μm) are 5 cm in daytime conditions, increasing to 10 cm in good nighttime conditions. If we call this value r_{0REF}, then we may re-express Equation (2) as

$$\theta^2 = \left(\frac{1.22\lambda}{D}\right)^2 + \left(\frac{1.22\lambda_0}{r_{0REF}}\right)^2 \left(\frac{\lambda_0}{\lambda}\right)^{2/5} (\sin\alpha)^{-6/5} \quad , \tag{5}$$

where λ_0 is the wavelength for r_{0REF}.

For the system under analysis we have D = 60 cm; we will assume r_{0REF} to be 5 cm (λ_0 = 0.5 μm) at α = 90°. With these assumptions, the separate contributions of diffraction and turbulent seeing conditions to the size of an image are plotted against wavelength (for various elevation angles) in Figure 6. The resulting total image size is plotted in Figure 7.

We find that for the low elevation angles atmospheric turbulence is a very significant contributor to the size of the satellite images. In the MWIR (3–5 μm) band it is the main contributor, while for the LWIR (8–12 μm) band it is at least comparable to diffraction.

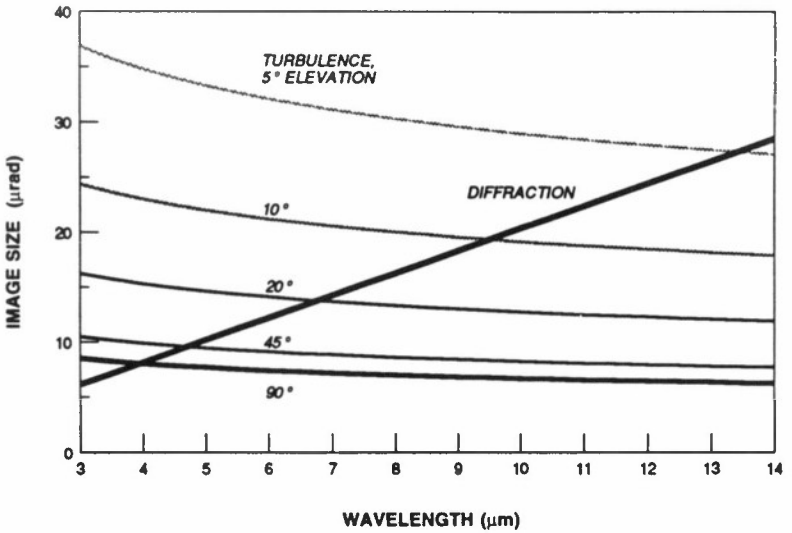

Figure 6. Contributions of diffraction and turbulence ("seeing") to image size vs. wavelength. Turbulence curves are for elevation angles 5–90°. Diffraction size is for 60-cm (24-inch) objective diameter.

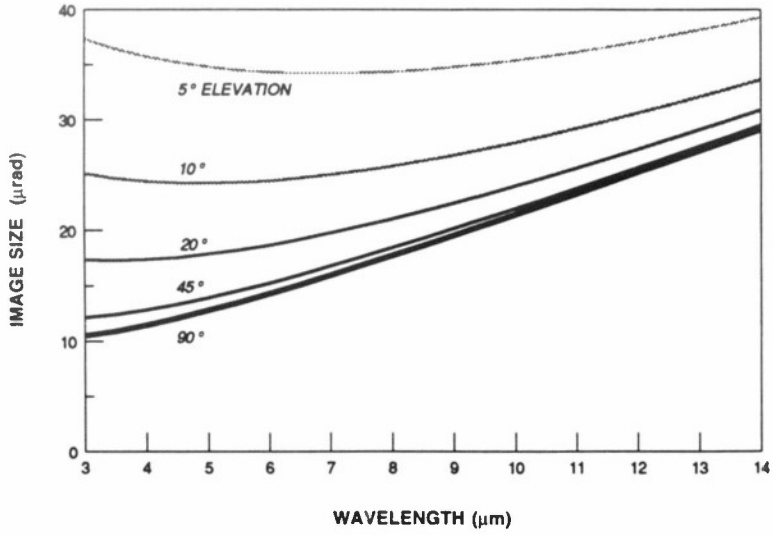

Figure 7. Total size of point-source image vs. wavelength for elevation angles 5–90°.

4. SYSTEM DESIGN

The essential elements of a system for infrared acquisition and tracking of satellites are shown in Figure 8. Details of the special subsystems and operating procedures are discussed in the following sections.

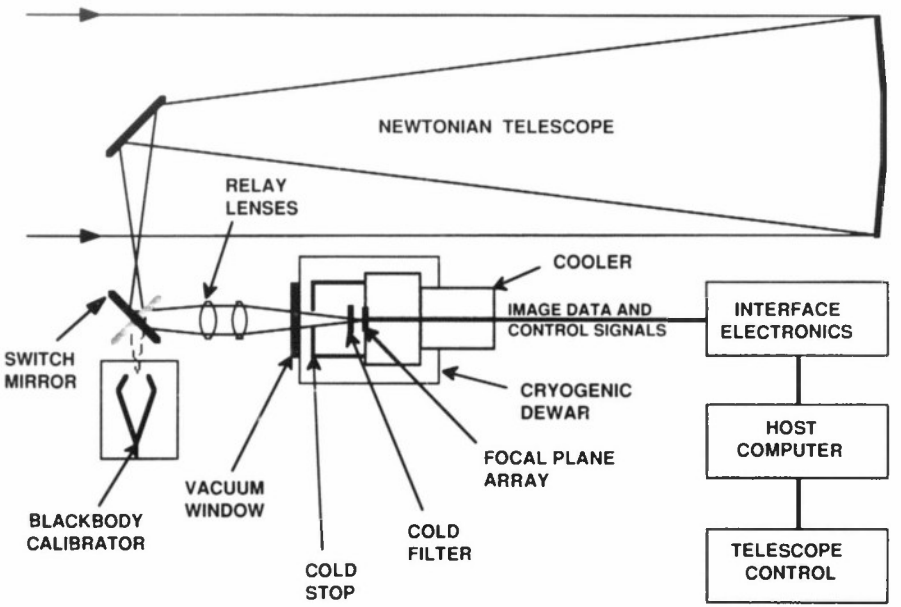

Figure 8. Schematic diagram of an infrared satellite acquisition system.

4.1 OPTICAL ELEMENTS

The numerical calculations which follow are based on use of a 60-cm Newtonian telescope such as the auxiliary telescope of the Firepond Observatory. As may be seen from Figure 6, this aperture is sufficient to give diffraction-limited images comparable to or smaller than the atmospheric seeing disk. Additional optics will be included to provide a suitable effective focal length for the focal plane array and to ensure effective cold-stopping and baffling to reject stray radiation.

4.1.1 Primary and Diagonal Mirrors

The primary mirror has a diameter of 0.60 meters and a focal length of 3.25 meters. The collecting area is 0.27 m^2 after allowance for obscuration by the diagonal flat mirror.

4.1.2 Relay Lenses

A relay lens assembly provides the desired effective focal length. The total field of view of the FPA should be large, to allow maximum integration time for each possible satellite position; this suggests the use of the shortest practical effective focal length. The effective focal length is chosen so that the image size is approximately one pixel. Detectors much larger than the satellite image will receive more background radiance than is necessary, leading to a decrease in the SNR. Furthermore, if the satellite image were much smaller it could sometimes fall on the nonresponsive spaces between detectors.

A longer focal length would lead to greater precision in tracking after initial acquisition. The SNR need not be adversely affected by an increase in image size to several pixels, provided that the system electronic noise and readout noise are small compared to the background photon noise, i.e., the detector is background-limited. However, because the present study is primarily concerned with acquisition, we will assume that maximum field of view is the most important consideration.

For operation at low elevation angles, the image size typically will be 25 μrad for all IR wavelengths of interest (see Figure 7). The typical pixel pitch of the available FPAs is 50 μm. Thus, the effective focal length should be about 2 meters, which gives an effective f/number for the 60-cm telescope of f/3.35. The magnification of the relay optics is 2/3.25, or 0.615.

4.1.3 Cold Stop and Baffling

The introduction of the relay lens provides a simple way to locate a cold stop so that only desired radiation from the optical aperture is received at the focal plane. An image of the primary mirror appears between the relay lens and the focal plane. This is to be located inside the dewar; a cold stop is placed there. The cold stop structure is to include a central obscuring disk located at the image of the diagonal mirror. Other cold masking elements block radiation from the diagonal supports.

Cold baffling elements in the dewar should be designed to trap stray radiation before it can be scattered onto the FPA. Objects outside the dewar which are above ambient temperature should be shrouded from the optical path.

4.1.4 Cold Filter

Depending on detector characteristics, a cold passband filter should be included in the dewar to tailor the system response to just those wavelengths which are transmitted, not radiated, by the atmosphere. Simulation calculations have been performed to choose the best passband to maximize the SNR.

4.1.5 Optical Transmission

We will assume the reflectivity of the telescope mirrors to be 95 percent and emissivity to be 5 percent. Refractive optical elements, such as germanium lenses with multilayer antireflection coatings, are expected to transmit 95 percent. If we allow for three elements in the relay lens, plus the dewar window, we estimate that the overall optical transmission τ_O = 74 percent. (The cold filter is treated separately.)

4.1.6 Emission of Optical Elements

Appendix A shows that the effective thermal emissivity of the optical elements at ambient temperature, as seen by the FPA, is given approximately by

$$\varepsilon_{EFF} = 1 - \prod_{1}^{n} \tau_i = 1 - \tau_O \quad . \tag{6}$$

Thus, given the assumptions above, we find the value of 0.26 for ε_{EFF}. At 295 K, the total blackbody radiance from the optical surfaces is thus 36 $Wm^{-2}ster^{-1}$.

4.1.7 Scattered Light

Another source of background radiation is ambient infrared light scattered from the optical surfaces. We would need to know the bidirectional reflectance distribution function (BRDF) of each surface to evaluate this fully. For this study, we will assume that the condition of the surfaces is good enough that this background is small compared to the self-emission from the surfaces.

4.2 DETECTORS

Characteristics of a variety of IR FPA detectors which are commercially available or soon to be available are listed in Table 1. The indium-antimonide and mercury-cadmium-telluride detectors are arrays of photodiodes connected to readout multiplexor arrays by indium-bump bonds. They are available from Amber Engineering, Inc. and other manufacturers. The parameters of these detector arrays are based on those of a 128 × 128-element array already available from Amber Engineering [4]. Also developed by Amber is the gallium-doped silicon array with a similar readout, which operates as a photoconductor. For comparison, we list platinum-silicide and iridium-silicide Schottky-barrier detectors. Although they have relatively low quantum efficiencies, their monolithic silicon construction and CCD readout structures offer high uniformity, good pixel yield, and low noise. The properties listed for the PtSi Schottky array are based on those of PtSi cameras produced by David Sarnoff Research Center [5]. The data for the IrSi array are based on detectors produced jointly by Lincoln Laboratory and Ford Aerospace [6,7,8]. Approximate responsivities of the detectors listed in Table 1 are plotted in Figure 9. The model parameters have been adjusted, where possible, to match measured characteristics.

TABLE 1

Properties of Infrared Focal Plane Arrays

Type of detector	InSb	HgCdTe	Si:Ga	PtSi	IrSi
Mode	PV	PV	PC	PV	PV
Cutoff wavelength (μm)	5.5	10.5	19.1	~ 5	9.4
Operating temp. (K)	80	55	20	80	40
Rows × columns	256 × 256	128 × 128	128 × 128	244 × 160	256 × 256
Pixel pitch (μm)	50	50	50	80	40
Filling factor	~ 90 %	> 64 %	~ 100 %	39 %	52 %
Quantum efficiency	53 %	~ 40 %	~ 12 %	~ 1 %	~ 1 %
Readout noise (e^-/pixel)	800	1,600	1,600	300	300
Max. charge (e^-/pixel)	4×10^7	4×10^7	4×10^7	1.2×10^6	1.2×10^6
Good pixel fraction	99 %	< 97 %	> 97 %	99.9 %	99.9 %
Uniformity	3.5 %	~ 5%	~ 5%	~ 2%	~ 2%

4.3 CALIBRATION SOURCES

The responsivities of the detectors in a staring FPA typically vary by about 3–5 percent. In addition, there are various sources of DC offset from pixel to pixel. It is essential to correct the output of the array for these gain and offset differences. For this purpose, a flat-field calibration source (or sources) should be included in the camera optics assembly. For calibration, a fold mirror in the optical train is rotated to a position such that radiation from the calibration source illuminates the focal plane uniformly. Just prior to each observation, camera signals are to be recorded for at least two different levels of illumination. These levels should closely bracket the actual illumination received from the sky during an acquisition search. An offset and gain factor are computed for each pixel; these are then applied to the raw digital readouts in real time. This is called a "two-point" correction if two illumination levels are used.

4.4 CAMERA INTERFACE ELECTRONICS

The stream of data from any of the IR FPAs considered in this study is voluminous, partly because each array contains 10^4–10^5 pixels in each frame. Furthermore, the relatively high sky-background radiance and limited charge-holding capacity of each pixel require the frame rates to be high (30–1,000 frames per second). If each pixel is digitized to 12 bits, the gross data rate is $\sim 4 \times 10^6$ to $\sim 10^9$ bits per second.

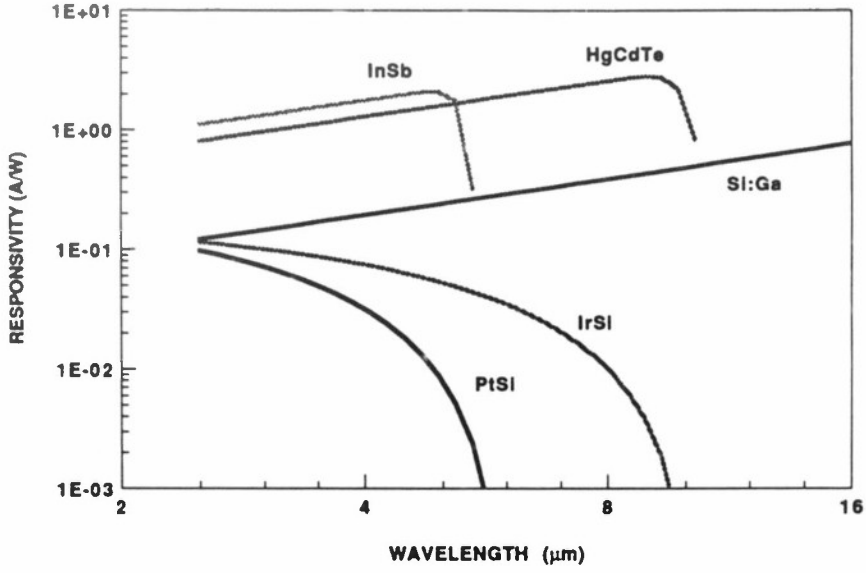

Figure 9. Numerically modeled responsivities vs. wavelength for some candidate FPA detectors.

For the acquisition of known satellites the telescope can track the nominal positions of the satellites. Thus, the satellites are nearly stationary within the field of view and a long integration time is permissible before the image data are sent to a processor for satellite detection. The sensitivity of the search increases with integration time.

From this information it appears advantageous to include a front-end processor in the camera interface electronics to integrate the image data as it comes from the focal plane. At its minimum, the processor would receive digital data at the camera frame rate, sum the frames N at a time, and produce output data at $1/N$ of the camera frame rate. Other functions should be included, such as pixel-by-pixel correction for responsivity and offset variations and provision of a standard composite video signal for real-time displays. The data summation provided by the front-end processor must not be confused with data sampling to provide a lower frame rate. The latter process does not provide the long integration times which are needed here. An output rate of 30 frames per second or less should be manageable in the subsequent processors. The interface electronics should also include scan-conversion circuitry to produce a standard composite video signal for real-time displays. In addition, commercial video-processing equipment may be used to advantage.

4.5 HOST COMPUTER

The acquisition system must include a host computer (or computers) to operate effectively in real time. Tasks handled by the host include pointing the telescope toward the satellite, controlling its tracking rates, and processing the IR images to sense the presence of the satellite above the background noise. Other tasks may be performed, such as automatic camera calibrations and interactions with the system operators. However, real-time image displays should also be provided so that human operators may monitor the operations. An alert human can probably make a better judgment of the reality of a suspected satellite detection than a computer algorithm can.

4.6 ACQUISITION PROCEDURE

For this study it is assumed that the orbital parameters of the satellite are approximately known. The satellite will be within a given radius of the predicted nominal position (see Figure 3). This uncertainty radius, and the range vector to the nominal position, defines an angular search box which moves with the satellite and grows as the satellite approaches. On the basis of the expected IR signature of the satellite, an elevation angle is chosen which gives a high probability of detection in the initial search.

Sky-background data are recorded immediately prior to an acquisition observation. This would be done at the same elevation and azimuth angles as the nominal acquisition search. Thus, the level and spectrum of sky radiance should be the same as for the actual search. The averaged background data are then subtracted from the averaged search frames.

The box is to be searched at a nearly constant elevation angle by scanning the camera in azimuth across the search box during the time the satellite elevation increases by the height of one camera field of view (FOV). At the same time, the camera elevation will move with the nominal elevation of the satellite. The azimuth scan is repeated, one FOV lower each time, until the whole box has been searched.

The real-time image processing during the search basically consists of averaging the IR signal received from each pixel fixed with respect to the search box. The processor tests for a pixel with a signal significantly above background after the maximum allowed integration time. The detailed nature of the scan, whether step-and-stare or continuous motion, will depend on the capabilities and limitations of the available hardware and software. A smooth scan is preferred so that time is not lost waiting for the telescope motion to settle before staring at each new field. However, more real-time computational power is needed to integrate the signals from points which appear to move across the focal plane.

Once a probable satellite detection has been made in one FOV, the telescope controller is instructed to stop scanning and new integrations are commenced on the same field of view. If the second integration fails to show a significant signal, a "false alarm" is declared and the search resumes at the next FOV. This practice of taking a second look at a suspected satellite permits us to lower the detection threshold, as a much higher false-alarm rate per FOV may be tolerated than if only one pass over the search box were permitted.

If the satellite has not been discovered by the time the box has been completely searched, a new search begins, this time with recomputed parameters of range, elevation, search box size, and integration

times. The new search should be more sensitive because the satellite is closer and at a higher elevation angle the second time.

4.7 INFRARED TRACK AFTER ACQUISITION

The staring FPAs are well suited to tracking the satellite once it has been acquired. The telescope would be pointed directly at the detected satellite, and a tracking algorithm determines the satellite image centroid after each integration period. The error signals thus obtained are used to keep the system pointed at the satellite. The angular uncertainty in the tracking signals will be roughly the angular size of the satellite image divided by the SNR of the detection. The bandwidth of the tracking signals will correspond to the integration time in use. Further analysis of tracking is beyond the scope of this report.

5. PERFORMANCE ANALYSIS

5.1 RANGE EQUATION

The goal of this analysis is to determine whether a given satellite can be detected reliably at the necessary range by a proposed system. Reliable detection means that the satellite signal S must be larger than the total system noise N by a factor sufficient to ensure a high probability of detection P_D while permitting a low rate of false alarms K_{FA}. A detection threshold is set at X times the noise level, where X is determined from K_{FA} and the normal probability integral (assuming that the system noise follows a Gaussian distribution). The signal must be above XN by some amount YN to ensure a high probability of detection P_D. Finally, the required SNR Z_{MIN} is X plus Y.

An analysis of the required SNR is presented in Appendix C. There we show that a value for Z_{MIN} of 6 yields a detection probability of 95 percent, while the false alarm rate is 12 percent per FOV. As discussed in Section 4.7, a relatively high rate of false alarms is tolerable because the search procedure allows us to take a second (and third) look at a suspected satellite detection.

A figure of merit often cited for infrared detectors is the normalized detectivity D^*. Such a quantity is often useful in finding the SNR for detectors proposed for a given application. However, the value of D^* depends on the background flux, which is responsible for a major component of noise. In the present case, we prefer to calculate the photon background and use a direct measure of the other sources of noise, such as noise-equivalent input power or zero-flux readout noise. D^* is discussed further in Appendix D.

5.1.1 Signal

The total signal from the satellite, in photoelectrons, may be estimated from

$$S = \frac{A_T \tau_O Q t_{INT}}{4\pi R^2} \quad , \tag{7}$$

$$Q = \frac{1}{hc} \int_{\lambda_1}^{\lambda_2} \lambda I_{S\lambda} \tau_A(\lambda) \tau_F(\lambda) G \eta(\lambda) d\lambda \quad , \tag{8}$$

where

$I_{S\lambda}$ = spectral radiant intensity (infrared signature) of the satellite (W/ster μm),

A_T = collecting area of the telescope (m^2),

R = range to the satellite (m),

hc = Planck's constant times the speed of light = 1.24 eV·μm,

τ_O = average transmission of the receiving optics,

$\tau_A(\lambda)$ = transmission of the atmosphere,

$\tau_F(\lambda)$= transmission of receiver passband filter,

$\eta(\lambda)$= quantum efficiency of the detector,

λ_1, λ_2 = limiting wavelengths of the filter-detector combination,

G = photoelectric gain of the detector (= 1 for photovoltaic devices),

t_{INT} = integration time on each pixel in the search box,

and all of the important wavelength dependencies are explicitly shown.

5.1.2 Noise

The total system temporal noise N for one integration period is given, in electrons, by

$$N^2 = n_B^2 + n_E^2 \quad , \tag{9}$$

where

n_B = the quantum noise of detected background photons including (for photoconductors) generation-recombination (G-R) noise, and

n_E = electronic noise from the detector, preamplifiers, etc.

The background photon noise (Poisson noise) contains contributions from both the sky radiance and emission of the telescope optics:

$$n_B^2 = B + B_T \quad . \tag{10}$$

Quantum noise. The number of photoelectrons in each unresolved point image produced by the background sky radiation is given by

$$B = A_T \omega \tau_O Q_A t_{INT} \quad , \tag{11}$$

$$Q_A = \frac{1}{hc} \int_{\lambda_1}^{\lambda_2} \lambda L_{A\lambda} \tau_F(\lambda) G \eta(\lambda) d\lambda \quad , \tag{12}$$

where the symbols are as defined before, except

$L_{A\lambda}$ = spectral radiance of the atmosphere, and

ω = total solid angle of the satellite image.

The solid angle ω includes not only the contributions of diffraction, atmospheric turbulence, and telescope aberrations (adding up to the optical image size ω_i), but also ω_{pix}, the size of the discrete detector pixels. The angular size of the total image results from the convolution of the point-spread functions from the individual contributions, each of which can be characterized by a variance. The variance of the convolved image is the sum of the individual variances. Because the variances vary as the squares of the

angular sizes, they vary directly with the solid angles of the individual contributions. By this heuristic reasoning, we may simply add the solid angle contributions

$$\omega = \omega_i + \omega_{pix} \quad , \tag{13}$$

$$\omega_{pix} = \frac{A_{pix}}{f^2} \quad , \tag{14}$$

where

f = the effective focal length of the telescope and

A_{pix} = the area of one pixel in the focal plane.

The additional background current caused by radiation of the optical elements is calculated from

$$B_T = A_T \omega \varepsilon_{EFF} Q_T t_{INT} \quad , \tag{15}$$

$$Q_T = \frac{1}{hc} \int_{\lambda_1}^{\lambda_2} \lambda L_{T\lambda}\, \tau_F(\lambda) G\, \eta(\lambda) d\lambda \quad , \tag{16}$$

where

$L_{T\lambda}$ = spectral radiance of a blackbody at the temperature of the telescope,

ω = solid angle subtended by a satellite image, as before, and

ε_{EFF} = the effective emittance of the telescope optics (Equation (6)).

The total quantum noise power is thus given by

$$n_B^2 = A_T \omega \left(\tau_O Q_A + \varepsilon_{EFF} Q_T \right) t_{INT} \quad . \tag{17}$$

Electronic noise. Sources of electronic noise include Johnson noise in the detector, shot noise from detector dark current, noise from the readout process, and preamplifier noise. Rather than attempting to isolate and estimate each of these sources, we have used measured values of the noise-per-pixel readout, obtained in conditions of minimal photon flux on the detectors. These noise values are listed in Table 1. For the ground-based sensors of this study, we find that the quantum noise from background photons is the dominant term, in any case.

Many pixel readouts are summed, in general, to obtain a single integration of satellite signal. The summation is over individual frames which are read during the integration time and over the number of pixels which encompass the satellite image. The electronic noise is thus given by

$$n_E^2 = m_\Sigma N_{RI}^2 F t_{INT} \quad , \tag{18}$$

where

m_Σ = number of pixels summed to include the image of the satellite

$$m_\Sigma \geq \frac{\omega}{\omega_{pix}} = 1 + \omega_i \frac{f^2}{A_{pix}} \quad , \tag{19}$$

N_{RI} = total electronic noise (in electrons) for a single pixel readout, and

F = frame rate (sec^{-1}), assuming that Ft_{INT} = 1, 2, 3,... .

Total temporal noise. If we add together all of these contributors, we find the expression for the total temporal noise is

$$N_{TEMP}^2 = \left(A_T\omega\left(\tau_O Q_A + \varepsilon_{EFF}Q_T\right) + m_\Sigma N_{RI}^2 F\right)t_{INT} \quad . \tag{20}$$

Quantization noise. In order to perform the signal summations mentioned above, the analog pixel readouts are first converted to digital form. The analog-to-digital (A/D) converter will have enough resolution for this task if the least-significant-bit (LSB) step size Δ (here, in units of electrons) is less than approximately twice the RMS temporal noise in the analog signals. The RMS quantization error for a single readout is

$$n_Q = \frac{\Delta}{\sqrt{12}} \quad . \tag{21}$$

The quantization noise for the summed frames is given by

$$N_Q^2 = m_\Sigma \frac{\Delta^2}{12} F t_{INT} \quad . \tag{22}$$

As long as $t_{INT} >> 1/F$ we can treat the quantization noise as a part of the temporal electronic noise, and the total noise becomes

$$N^2 = N_{TEMP}^2 + N_Q^2 = \left(A_T\omega\left(\tau_O Q_A + \varepsilon_{EFF}Q_T\right) + m_\Sigma\left(N_{RI}^2 + \frac{\Delta^2}{12}\right)F\right)t_{INT} \quad . \tag{23}$$

Spatial Noise. In addition to temporal noise and quantization noise, we must consider spatial noise, often called fixed-pattern noise. Unlike temporal noise, spatial noise bears a fixed ratio to the total signal plus background, independent of integration time. Spatial noise sets a lower limit to the strength of signals which can be detected, even with unlimited integration time; it arises from individual variations in the responsivity and offset of each detector in the array. In general, these variations cannot be calibrated perfectly[9].

However, the present application permits us to minimize some of the sources of spatial noise. First, the background radiance responsible for practically all the photocurrent should be quite smooth over the angular scales of interest here. Many frames of such background can be recorded and averaged within minutes of the expected appearance of the satellite. Furthermore, this will be done for the same patch of sky to be searched. Both the magnitude and spectral distribution of this background radiance should be unchanged during the acquisition search. Thus, two of the sources of spatial noise in the detectors, i.e., differential nonlinearities and differential spectral response, are nullified when the average background frame is subtracted from each search frame. One source remains, which we are unable to evaluate without experience with the actual detector systems. This is excess low-frequency, or "1/f," noise in the detectors. This type of spatial noise causes the irregularities to grow as the logarithm of the time since the reference frames were recorded.

To measure and adequately correct for both the detector responsivities and the sky backgrounds, the camera signals must be converted to digital form with great accuracy. Not only must the quantization noise be small, but irregularities in the signal thresholds for each digital output value (differential nonlinearities) in the A/D converter(s) must be kept to a minimum [10]. At present, most of the A/D converters which can operate at the speeds required for these focal planes have a precision of just 12 bits; this probably accounts for reports that the minimum achievable spatial noise for HgCdTe detector arrays is roughly 0.03 percent [11]. We wish to develop a system in which the the A/D errors are small enough not to introduce significant spatial noise. Averaged frames will have to be stored with more bits of precision than are provided by the A/D converters.

In infrared astronomy, the procedure generally used to obtain accurate measurements of the flux from a point source is to move a single detector optically on and off the source and measure the difference in signal; the background radiance is thus subtracted out. A staring sensor uses separate detectors to make the on-source and off-source measurements simultaneously. If the spatial noise in the array is too great, however, the search procedure could be modified to scan the array smoothly across the search box while the photon signals are integrated in computer memory, as in a time delay and integration (TDI) sensor.

Three lessons are to be learned from a consideration of spatial noise. First, the detectors should be as uniform as possible. Second, the wavelength passband of the cold filter should be carefully chosen to minimize the background radiance, which will be multiplied by the spatial noise factor, without unduly reducing the satellite signal. Third, the A/D converters must be accurate enough to obtain many-frame averages of high precision.

For the present analysis, we will assume the spatial noise to be equal to the residual temporal noise in a one-second average of the background radiance. We wish to emphasize that only experience with the detector system will show whether spatial noise can actually be reduced this low.

Clutter. There can also be real irregularities in the background, called clutter, which have a similar effect on the detection limits of the system. In this application, stars are one form of clutter. From the results of the Infrared Astronomical Satellite (IRAS) survey [12], the density of sources in the 12-μm band at high galactic latitude with spectral flux densities above 0.5 Jansky is approximately 0.6 per square degree (1 Jansky = 10^{-26} W m^{-2} Hz^{-1}). The number of sources above a given flux level decreases as the −1.0 power of the flux level. The most sensitive detector system considered so far (HgCdTe) may be able to detect a satellite of 100 W $ster^{-1}$ at a distance of 4400 km at 10° elevation angle (in a typical engagement). This corresponds to a flux level in the 12-μm IRAS band of 41 Janskys. The corresponding density of sources is 0.0073 deg^{-2} at high galactic latitude, but greater than 0.3 deg^{-2} within a few degrees of the galactic plane. A satellite position uncertainty of ± 50 km at 4400 km leads to a search box of 1.7 deg^2. The chance that an IR star as bright as the satellite will appear in the box thus ranges from ~ 1 percent over most of the sky to ~ 50 percent in the galactic plane. The satellite would still be distinguishable by its motion but the possible presence of stars must be considered in the design of the search algorithms.

Atmospheric turbulence already discussed in Section 3.3, results in a form of clutter called sky noise. This is not to be confused with the Poisson noise of arriving background photons. This phenomenon arises from fluctuations in temperature and water-vapor density, described by C_T^2 and C_w^2, which

each affect the local atmospheric radiance. Observations of sky noise with individual detectors indicate that the overall RMS amplitude is about 10^{-4} of the average sky radiance.[13] However, we will only be concerned with the variations over angular scales of ~20 to ~100 μrad. Some of this variation may also be averaged out as the satellite is tracked across the sky.

A very unpredictable form of clutter is from clouds. High, thin cirrus clouds, which may not even be visible to the eye, can cause great difficulty in attempting to establish the sky background level. In addition, they attenuate the satellite signal by an unknown factor. In this report, all calculations assume clear sky conditions, i.e., no clouds present.

Finally, other satellites, or even aircraft, could be confused with the satellite of interest. It is assumed here that as soon as a candidate detection is made a track will be established; it will be rejected as clutter unless the motion parameters reasonably match those expected of the satellite.

5.1.3 Maximum Range of Detection

If we know the system noise level N and have determined the required SNR Z_{MIN} (= S/N), we can use Equation (7) to find the maximum range of detection:

$$R = \sqrt{\frac{A_T \tau_O Q t_{INT}}{4\pi Z_{MIN} N}} \quad . \tag{24}$$

In the background-limited case ($n_B >> n_E$), we can use Equations (9), (17), and (6) to find

$$R^2 = \frac{Q\tau_O}{4\pi Z_{MIN}} \sqrt{\frac{A_T t_{INT}}{\omega\left[\tau_O Q_A + (1-\tau_O) Q_O\right]}} \quad . \tag{25}$$

It may be observed from these equations that the maximum detectable range is a relatively insensitive (fourth-root) function of parameters such as telescope collecting area, integration time, or background radiance.

5.2 VALUES OF SYSTEM VARIABLES

General system parameters used in the performance calculations are summarized in Table 2. Parameters optimized for each type of focal plane array are listed in Table 3.

5.2.1 Signal and Noise Levels

To estimate the signal and noise levels for a typical satellite, we have carried out the integrations for Q, Q_A and Q_T, Equations (8), (12), and (16), using the characteristics of each type of detector as summarized in Table 1. For Q, a reference satellite spectral radiant intensity $I_{S\lambda}$ was computed for a projected-area emittance product of 5 m^2, with a temperature of 300 K. The assumed range was 1000 km. The background sky radiance for calculation of Q_A is as shown in Section 3.1 for clear, midlatitude summer sky. Table 3 lists the minimum camera frame rates required to avoid saturation of the detectors.

TABLE 2

Basic System Parameters Used In Performance Calculations

Telescope parameters	
Collecting area	0.272 m^2
Optical transmission	0.74
Effective emittance of optics	0.26
Temperature	300 K
Atmospheric coherence length ($\lambda = 0.5$ μm, zenith)	5 cm
LOWTRAN7 parameters	
Atmospheric model	Midlatitude, summer
Aerosol model	Rural
Visibility range	23 km
Satellite position uncertainty radius	50 km

TABLE 3

Parameters for Different Focal Plane Arrays

Camera type	InSb	HgCdTe	Si:Ga	PtSi	IrSi
Effective focal length (m)	2.5	2.0	2.0	2.5	1.6
Relative aperture (f/#)	4.19	3.35	3.35	4.19	2.68
Field of view (mrad)	5.12	3.20	3.20	3.9 × 5.12	6.40
FPA solid angle ($\times 10^{-6}$ ster)	26.2	10.2	10.2	20.0	41.0
Filter cut-on wavelength (μm)	3.4	8.4	8.4	3.4	3.4
Filter cut-off wavelength (μm)	4.1	9.4	12.0	4.1	4.1
Maximum pixel current (pA)	47.3	4681	3190	1.36	3.45
Minimum frame rate (sec^{-1})	10	1000	500	10	20

The detector signal currents resulting from this reference satellite are plotted as a function of elevation angle in Figure 10. Figure 11 shows the DC sky radiance currents vs. elevation angle plus the telescope background radiance current. The solid-angle factor for these plots equals the size of the image plus the size of one pixel. The noise current density (in electrons/$\sqrt{sec}$) caused by these backgrounds is shown in Figure 12.

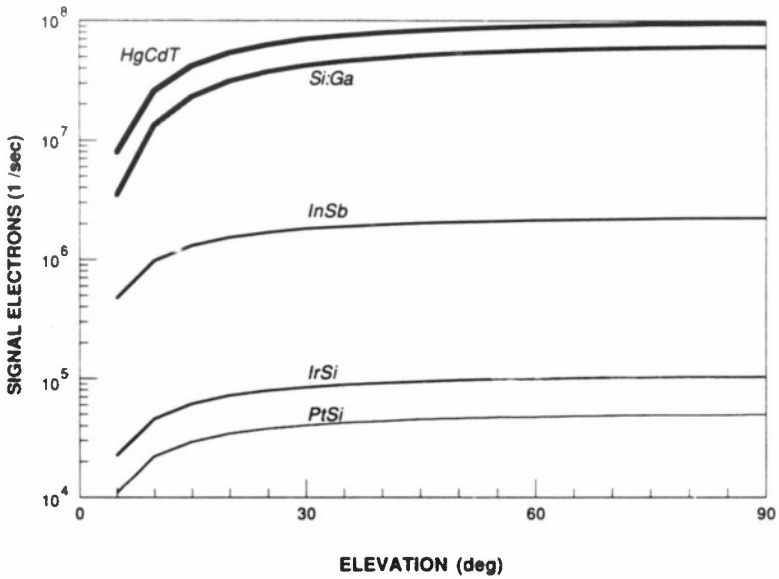

Figure 10. Signal current vs. elevation angle for various focal plane detectors. Assumed satellite has a projected-area emittance product of 5 m^2, temperature of 300 K, and a distance of 1000 km.

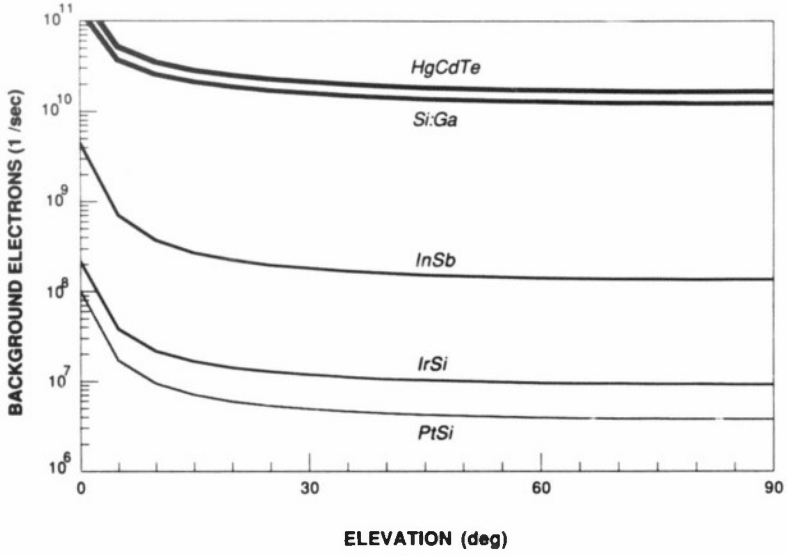

Figure 11. Total background currents vs. elevation angle within the solid angle subtended by an unresolved object.

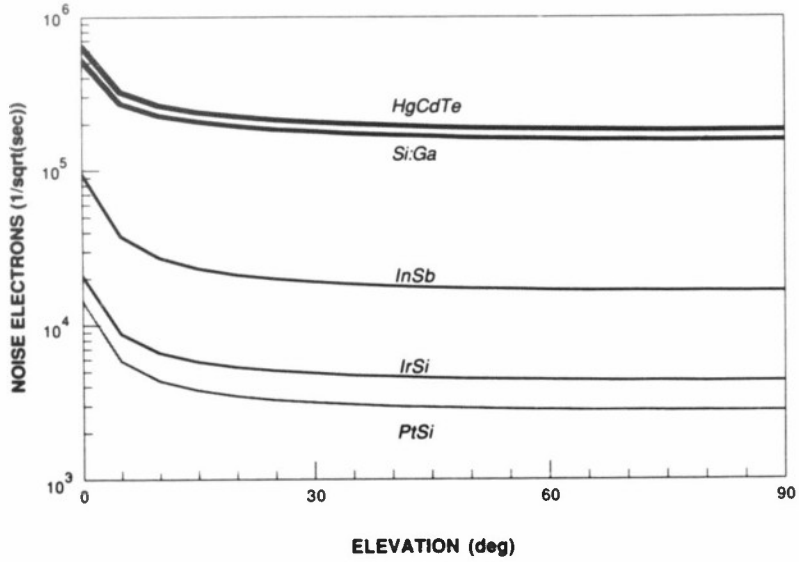

Figure 12. Noise electron current per image area vs. elevation angle for various detectors. Readout noise has been included.

5.2.2 Integration times

The integration time is limited to the amount of time that the telescope can be allowed to dwell on a single FOV within the area of sky to be searched. This maximum integration time on any point in the search box is the same whether the telescope scans smoothly across the box or steps quickly from field to field.

In order to carry out the satellite search at a given elevation, the scan across the horizontal width W of the search box must be completed in the time it takes for the satellite to rise in elevation by the height $\Delta\alpha$ of one FOV. The fraction of the horizontal scan which is spent on any one FOV is equal to the width $\Delta\phi$ of the FOV divided by W (assuming $W \geq \Delta\phi$). The equation is

$$t_{INT} = \frac{\Delta\alpha}{(d\alpha / dt)} \cdot \frac{\Delta\phi}{W} \quad , \tag{26}$$

where

$d\phi/dt$ = the elevation component of the angular velocity of the satellite.

The angular velocity of the satellite may be calculated from its orbital parameters and its position with respect to the observer. Assuming a circular orbit, t_{INT} may be found for any position of the satellite. The equations are given in Appendix B for the case of a satellite in a circular orbit passing overhead. Typical values of t_{INT} as a function of satellite position are plotted in Figure 13. For that figure, it is assumed that the camera FOV is 3.2 mrad square and the satellite position uncertainty radius is 50 km. For detection at the ranges of greatest interest, t_{INT} should be several tenths of a second. Notice that the background radiances will cause the detector charge capacities to be filled in much shorter times. Therefore, to take advantage of the possible integration times many frames of pixel data will have to be summed.

Notice that t_{INT} depends directly on the product $\Delta\alpha\Delta\phi$, which is the solid angle of the FOV. By design, the solid angle of a single pixel matches the optical image size determined by turbulent seeing and diffraction. Thus, the integration time is proportional to the number of pixels (detector elements) in the FPA. This is a general result which holds for scanning systems as well as purely staring systems.

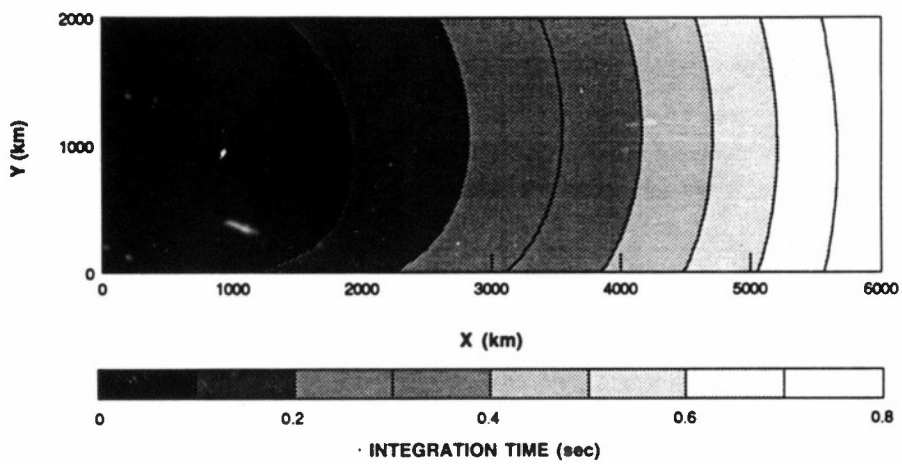

Figure 13. Typical contours of integration time vs. satellite position. For this plot, the relevant system parameters are satellite position uncertainty radius = 50 km, camera FOV = 3.2 × 3.2 mrad.

5.3 MAXIMUM RANGE VS. ELEVATION

We have compared the performance of the various FPAs for detecting satellites. A set of spreadsheet files was set up to find the SNR for a given satellite, as a function of satellite position, for each of the cameras. The appropriate system parameters, as well as could be determined, were used for each different focal plane. For simplicity, all satellites were assumed to be in circular orbits passing overhead. Integration times were taken to be a function of satellite position as described above. Two types of plots have been produced to show the results. Figure 14 is an X-Y plot of the positions of a reference satellite where the SNR would be 6. The Y axis is the observer's zenith direction and the X axis is the horizontal distance toward the rising satellite. The reference satellite was assumed to be at a temperature of 300 K and to have a projected-area emittance product of 5 m^2. This corresponds to a signature in the LWIR band of 192 W/ster. The curves show that the arrays with high quantum efficiency are capable of detecting such a satellite at extremely long ranges. HgCdTe is the best, with Si:Ga a fair second; InSb is still quite good. The Schottky-barrier silicide detectors are relatively inferior in this comparison. Nevertheless, Cantella [1] has shown that a PtSi sensor is quite useful in the space surveillance application. His results for the maximum range of detection are comparable to those presented here, though they were obtained by different methods.

5.4 MINIMUM SATELLITE SIGNATURE VS. POSITION

The second type of plot shows contours of minimum detectable signature as a function of position for a given detector. Once again $Z_{MIN} = 6$. In Figures 15–19, these threshold signature contours are presented for the various detectors, in W/ster in the appropriate wavelength band, 3–5 μm or 8–12 μm. In this way, the results may be used for satellites at a wide range of effective temperatures. (See Section 2.1 for the relationship between signatures in the different bands.) Overlaid on the contours are circular orbits at various altitudes and lines of constant elevation angle. Such a plot can be used to answer a number of different questions. For example, given a satellite altitude and IR signature, the plots show the minimum elevation angle at which the satellite is detectable with each FPA.

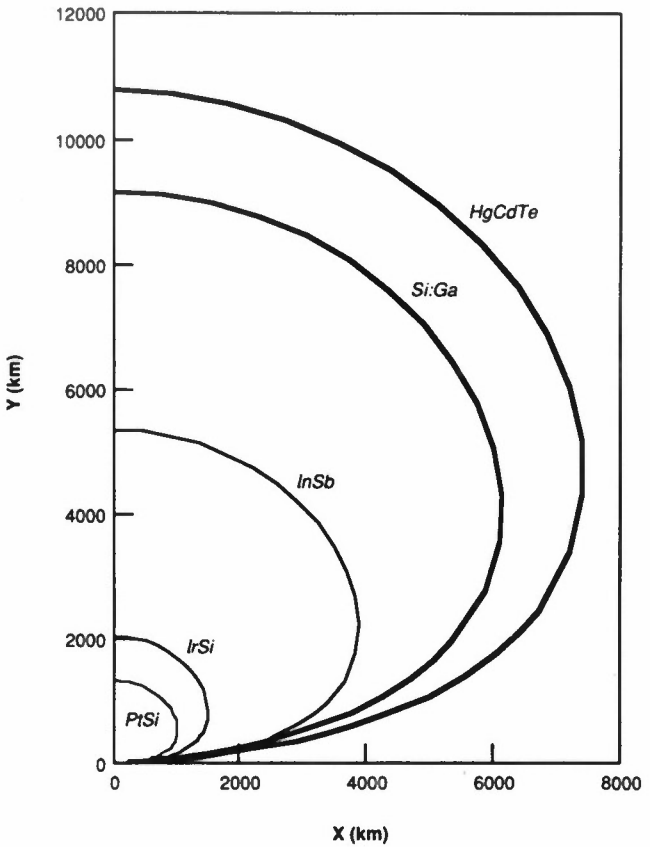

Figure 14. Zones of detection for different IR FPAs. The satellite is assumed to have a projected-area emittance product of 5 m^2 and a temperature of 300 K.

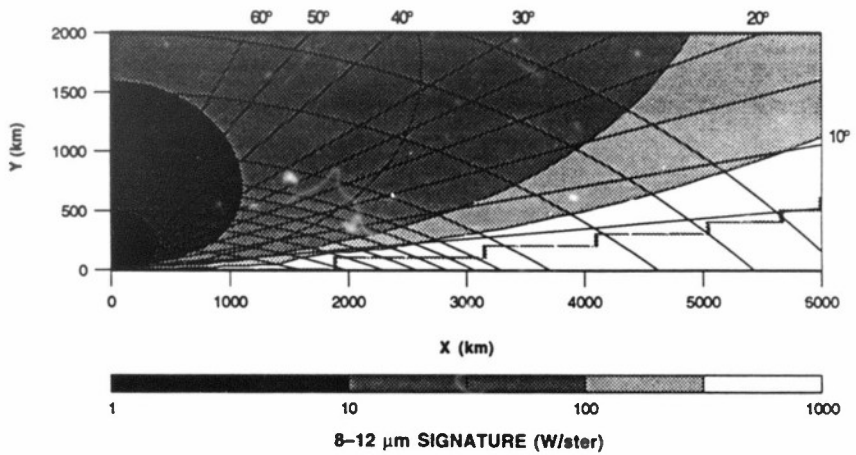

Figure 15. Minimum detectable in-band IR signature, as a function of position, for HgCdTe array (128 × 128). Signature units are W/ster in the wavelength band 8–12 μm (LWIR). Satellites are assumed to be passing overhead.

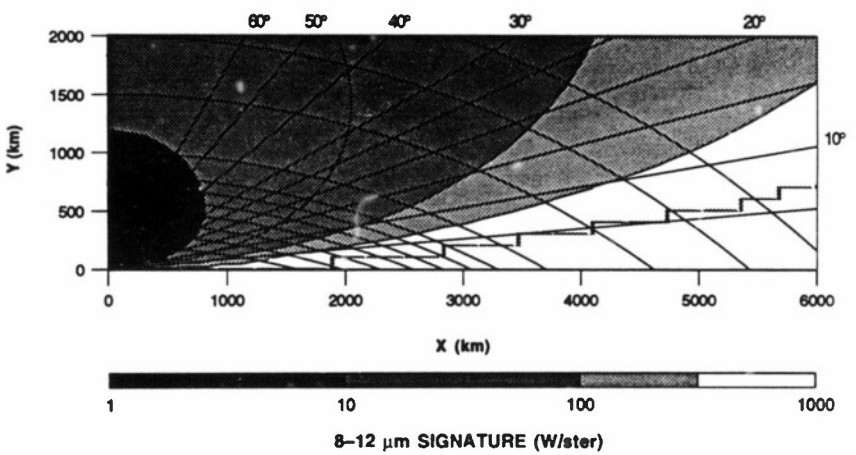

Figure 16. Same as Figure 15, but for Si:Ga array (128 × 128).

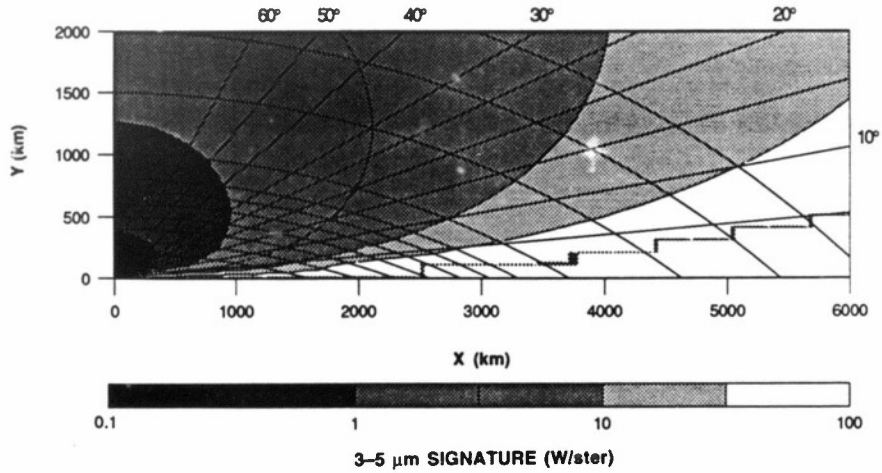

Figure 17. Similar to Figure 15, but for InSb array (256 × 256). The wavelength band here is 3–5 μm (MWIR).

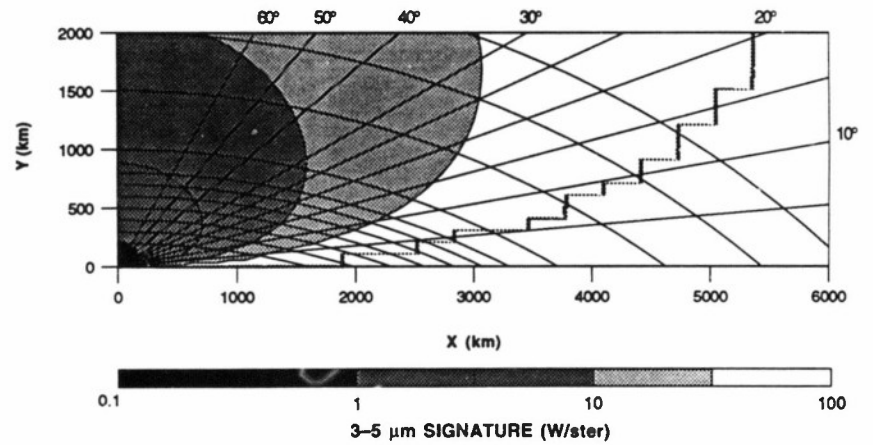

Figure 18. Same as Figure 17, but for IrSi array (256 × 256).

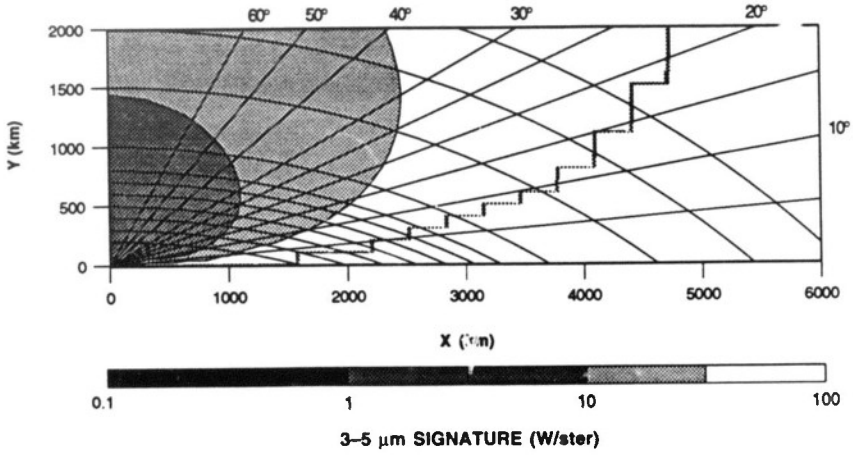

Figure 19. Same as Figure 17, but for PtSi array (160 × 244).

6. DISCUSSION AND CONCLUSIONS

All of the IR FPA detectors we have considered here show considerable promise for the acquisition of satellites whose orbits are approximately known. Predicted performance varies greatly, from that of the PtSi Schottky-barrier array to that of the HgCdTe array. The former could acquire medium-sized satellites at low altitudes, especially at high elevation angles; the latter can detect the smallest satellites at rather high altitudes or low elevation angles. All satellites are difficult to acquire at very low elevation angles. This may be seen in Figure 14, from the way all the signature contours approach the origin at low elevations. It is interesting to observe that the InSb array is ten times more sensitive than the PtSi array, which also operates in the MWIR band. This is to be expected, as the InSb array offers roughly 100 times the quantum efficiency of the Schottky-barrier detectors.

Factors other than theoretical performance may also weigh in the choice of FPAs. For example, the operating temperature of the array affects the cost and complexity of the cooling system required. We do not yet have sufficient data on the nonuniformities or 1/f noise of the arrays to evaluate spatial noise, though we expect this to have a significant effect on actual performance. The silicon-based arrays are expected to be superior in this regard, if only because the technology of silicon is better developed. Finally, there is the question of the producibility of each array and the percentage of usable pixels which can be expected. This last point is especially relevant to HgCdTe, as many years of development effort by the detector industry have not yet resulted in the ready availability of large arrays of these detectors.

For the proposed experiment, two of the candidate arrays appear most promising. In the MWIR band, the InSb array not only performs extremely well but is readily available. Even better performance can be found in the LWIR band. Here, the Si:Ga array looks very promising. Its theoretical performance does not quite match HgCdTe, but a working device has already been demonstrated by Amber Engineering; they have achieved a high yield of good pixels with good uniformity. Although HgCdTe could operate at higher temperatures and show higher responsivity, the higher technical risk to achieve a working system does not seem to be offset by these advantages. One complication of using the LWIR band is that the higher fluxes of background photons quickly saturate the charge-holding capacity of the pixels. Thus, the arrays must be read out at roughly 1000 frames per second. Digital circuits can be designed to integrate the frames in real time so that they can be presented to the host computer at a more manageable rate. On the other hand, MWIR detectors do not require frame rates in excess of 100 sec^{-1} to avoid saturation, and it may be possible to dispense with special frame-integrating hardware in that case.

Finally, altogether different arrays might be considered for IR satellite acquisition; for example, a linear array might be scanned in one direction to cover the same search box. The present analysis is applicable to many of these other cases. If the suggested detector has a quantum-efficiency curve similar to one of the arrays studied here, as far as theoretical performance is concerned the main difference is the total number of pixels in the array. The on-satellite integration time is proportional to this total number of pixels and the SNR varies as the square root of that number. For example, if we substitute a HgCdTe array having 480×1 pixels for one with 128×128 pixels, the integration time is reduced by

a factor of 34, the minimum detectable signal is increased by a factor of 5.84, and the range of detection of a given signature will be reduced by the square root of 5.84, or 2.42. This may still be adequate performance, and the linear array might offer offsetting advantages over the two-dimensional array.

The analyses contained in this report show that passive ground-based acquisition of satellites is feasible with IR FPAs within the present state of the art. The remaining uncertainties, such as the actual magnitude of spatial noise effects, can best be resolved by building a test system and operating it in the field. Such tests would provide a base of experience with different atmospheric conditions while yielding valuable measurements of real IR signatures of satellites.

APPENDIX A
EMISSION OF OPTICAL ELEMENTS

To estimate the thermal radiation from the optical elements, we set the emittance equal to the absorptance for the wavelengths of interest. For mirrors, the absorptance is 1 minus the transmittance. For lenses, light is either transmitted, absorbed, or reflected. If we assume that stray reflections from the lens to the detector come from surfaces at the temperature of the lens, then the surface reflectances may be added to the absorptance to obtain an apparent emittance. Thus the effective emittance is the complement of the reflectance or transmittance:

$$\varepsilon_i = 1 - \tau_i \quad . \tag{A-1}$$

The effective emittance of a series of optical elements (at one temperature) is found from a summation which includes the transmittances as well:

$$\varepsilon_{EFF} = \varepsilon_1 + \sum_{2}^{n}\left[\varepsilon_i \prod_{1}^{i-1} \tau_j\right] \quad , \tag{A-2}$$

which reduces to

$$\varepsilon_{EFF} = 1 - \prod_{1}^{n} \tau_i = 1 - \tau_{EFF} \quad . \tag{A-3}$$

APPENDIX B
ANGULAR SPEEDS OF SATELLITES

The angular speed of the satellite depends on its orbit, its range, and the angle of the line of sight relative to the orbital velocity vector. We can simplify the problem by assuming that the orbit is circular and that the ground track passes near the observer's position. Then for any given elevation angle α and range R, the elevation angular rate is known:

$$\frac{d\alpha}{dt} = \left[1 + \frac{R_E}{R}\sin\alpha\right]\frac{d\gamma}{dt} \quad , \tag{B-1}$$

where

R = slant range to satellite,

R_E = the radius of the earth, and

$d\gamma/dt$ = the angular speed of the orbit from the center of the earth. In radians per second, it is

$$\frac{d\gamma}{dt} = \frac{2\pi}{5036.9}\left(\frac{R_E}{R_E + H}\right)^{3/2} \quad , \tag{B-2}$$

where

H = the altitude of the satellite orbit.

APPENDIX C
REQUIRED SIGNAL-TO-NOISE RATIO

A search for a weak signal in the presence of noise must be guided by two requirements. The first is the maximum allowed rate (or probability) of false alarms K_{FA}. The second is the required probability of detection of a true signal P_D. In order to determine the required SNR Z_{MIN}, we also must know how many bins, or pixels, are to be searched for the signal. Call that number C. We assume that the noise is Gaussian with standard deviation N. The signal S is assumed to be small in relation to the average background, so that the bin containing the signal has the same level of noise as the background bins.

A detection threshold is to be set at a level xN above the background. A bin which exceeds this level is considered to contain a real signal. The false-alarm rate is computed as follows. The probability that noise in a single pixel will exceed xN is given by

$$p_1(x) = \frac{1}{2}\left[1 - I_{NP}(x)\right] \quad . \tag{C-1}$$

where I_{NP} is the normal probability integral

$$I_{NP}(x) = \frac{1}{\sqrt{2\pi}} \int_{-x}^{x} e^{-\frac{1}{2}t^2} dt \quad . \tag{C-2}$$

For small values of p_1 ($x > \sim 3$), it is useful to use a series expression:

$$p_1(x) = \frac{1}{x\sqrt{2\pi}} e^{-x^2/2}\left[1 - \frac{1}{x^2} + \frac{1 \cdot 3}{x^4} - \frac{1 \cdot 3 \cdot 5}{x^6} + \cdots\right] \quad . \tag{C-3}$$

The probability that no pixel will exceed xN is given by

$$1 - K_{FA} = \left[1 - p_1(x)\right]^C \quad . \tag{C-4}$$

If $p_1 << 1$, we have

$$\ln\left(1 - K_{FA}\right) = C \ln\left[1 - p_1(x)\right] \approx -C p_1(x) \quad , \tag{C-5}$$

$$K_{FA} \approx 1 - e^{-C p_1(x)} \quad . \tag{C-6}$$

If in addition $p_1 << 1/C$, we have simply

$$K_{FA} \approx C p_1(x) \quad . \tag{C-7}$$

The signal S must exceed the detection threshold by an amount yN sufficient to ensure a high probability of detection. The basic relationship is

$$P_D = 1 - \frac{1}{2}\left[1 - I_{NP}(y)\right] \quad . \tag{C-8}$$

In this case, it is easiest to use tabulated values of the normal probability integral to find a suitable y. Finally, the required signal level is given by

$$S = xN + yN \,, \tag{C-9}$$

$$Z_{MIN} = S/N = x + y \,. \tag{C-10}$$

In the satellite acquisition application, there is a very large number of pixels to be searched. If the range at acquisition is 1500 km with a position uncertainty radius of 50 km, then the search box is 33 mrad across. Typical image sizes of 25 μrad mean that roughly 2,000,000 pixels need to be searched. If we set $x = 5.6$, then we find $p_1 = 10^{-8}$ and K_{FA}= 2 percent. The false-alarm rate is a very steep function of x at this level. An SNR of 7 allows $y = 7 - x = 1.4$, which leads to P_D = 92 percent. Thus, we conclude that a satellite may be acquired with high probability and a low false-alarm rate if the SNR is 7 (~17 dB) or greater. A lower ratio such as 6 can be used and still give a high P_D, but only if a higher rate of false positives can be tolerated.

APPENDIX D

D^*

A figure-of-merit often quoted for various types of infrared detectors is the specific detectivity, written as D^*. It is defined as the SNR in a 1-Hz bandwidth per square root of detector area. The units of D^* are cm $Hz^{1/2}/W$. It is related to noise-equivalent power (NEP) by

$$D^* = \frac{\sqrt{A_D \Delta f}}{NEP} \quad ,$$

where

A_D = the area of the detector, or pixel (cm^2), and

Δf = the bandwidth (Hz).

In turn, NEP is related to the responsivity R (A/W), the RMS noise N (amperes), and the quantum efficiency η by

$$NEP = \frac{N}{R} \quad , \quad R = \frac{\eta}{h\nu} \quad ,$$

where $h\nu$ is the photon energy (eV).

To make use of D^*, we must also know the conditions to which a quoted D^* value applies: the incident wavelength or spectrum, the center frequency of the temporal passband, and the total incident flux, or solid angle in the case of a blackbody spectrum. Most frequently, D^* values are quoted for a 295 K blackbody incident spectrum, filling 2π steradians in front of the detector. Under such conditions, the NEP of a good IR detector should be dominated by the quantum noise of the detected photons. If so, it is said to be a BLIP (background-limited performance) detector. The D^* values are useful in comparing different detectors as long as the conditions of the proposed application are not very different from those for which the values are quoted.

If the detector is to be used in a low-background situation, then the quantum noise will be reduced. For example, reducing the FOV of the detector (increasing the f/number) will reduce the incident flux of background radiance as the sine of the half-angle of the cone of incidence. However, intrinsic noise sources may then become dominant. In applications for which the incident flux is low, or its spectrum is not a 295 K blackbody, it would be most useful if D^* values were given for a zero field-of-view, i.e., as if a cold shroud completely covered the detector. It would then be an easy matter to obtain the system noise floor of a proposed detector system to compare with the signals to be detected and the quantum noise of the expected photon background.

REFERENCES

1. M.J. Cantella, "Space surveillance application potential of Schottky-barrier IR sensors," MIT Lincoln Laboratory, Lexington, MA, Technical Report 772 (9 April 1987). DTIC AD-A180848.

2. F.X. Kneizys, E.P. Shettle, G.P. Anderson, L.W. Abreu, J.H. Chetwynd, J.E.A. Selby, S.A. Clough, W.O. Gallery, "Atmospheric Transmittance/Radiance — Computer Code LOWTRAN 7," Air Force Geophysics Laboratory (1988), Report No. AFGL-TR-88-XXX.

3. J.W. Goodman, *Statistical Optics*, Wiley-Interscience, 1985.

4. J.D. Blackwell, W.K. Johnson, A.R. Laband, H.R. Arnold, "Low-cost, high-performance 128 × 128 InSb focal plane array," *Proceedings of the IRIS Specialty Group on Infrared Detectors*, vol. 1, pp. 217–223, ERIM (Sept. 1989) [DTIC No. DLA900-88-D00392].

5. Walter F. Kosonocky and Gary W. Hughes, "High fill-factor silicide monolithic arrays," *SPIE Vol. 782*, pp. 114–120 (1987).

6. B-Y. Tsaur, M.M. Weeks, R. Trubiano, and P.W. Pellegrini, *IEEE Electron Device Letters*, vol. 9, pp. 650–653 (Dec. 88).

7. B-Y. Tsaur, M.J. McNutt, "IrSi Schottky-barrier focal plane arrays for long-wavelength infrared imaging," *Proceedings of the IRIS Specialty Group on Infrared Detectors*, vol. 1, pp. 245–255, ERIM (Sept. 1989) [DTIC No. DLA900-88-D-0392].

8. M.J. Cantella, N.C. Davison, C.H. Gylphe, J.P. Mattia, and B-Y. Tsaur, "Low-background application of Schottky-barrier IR sensors," *SPIE Vol. 1071*, pp. 12–30 (1989).

9. J.M. Mooney, F.D. Shepherd, W.S. Ewing, J.E. Murguia, J. Silverman, "Responsivity nonuniformity limited performance of infrared staring cameras," *Optical Engineering*, vol 28, pp. 1151–1161 (1989).

10. Analog Devices, *Data Conversion Products Databook*, pp. 3-9–3-14, 1989.

11. D. Spears, private communication.

12. C.A. Beichman, G. Neugebauer, H.J. Habing, P.E. Clegg, and T.J. Chester, *Infrared Astronomical Satellite (IRAS) Catalogs and Atlases, Explanatory Supplement*, Jet Propulsion Laboratory, 1984.

13. R. Papoular, "The processing of infrared sky noise by chopping, nodding, and filtering," *Astron. Astrophys.*, vol. 117, pp. 46–52, 1983; L.L. Smith and T.L. Herter, "A model for predicting infrared atmospheric emission fluctuations (sky noise)," *SPIE Vol. 551* "Adaptive Optics," pp. 131–139, 1985.

REPORT DOCUMENTATION PAGE

Form Approved
OMB No. 0704-0188

1. AGENCY USE ONLY (*Leave blank*)	2. REPORT DATE	3. REPORT TYPE AND DATES COVERED
	13 September 1991	Technical Report

4. TITLE AND SUBTITLE

Performance of Ground-Based Infrared Detectors for Acquisition of Satellites

5. FUNDING NUMBERS

C — F19628-90-0002
PE — 63221C
PR — 364

6. AUTHOR(S)

David R. Hearn

7. PERFORMING ORGANIZATION NAME(S) AND ADDRESS(ES)

Lincoln Laboratory, MIT
P.O. Box 73
Lexington, MA 02173-9108

8. PERFORMING ORGANIZATION REPORT NUMBER

TR-919

9. SPONSORING/MONITORING AGENCY NAME(S) AND ADDRESS(ES)

U.S. Army Strategic Defense Command
P.O. Box 1500
Huntsville, AL 35807-3801

10. SPONSORING/MONITORING AGENCY REPORT NUMBER

ESD-TR-91-080

11. SUPPLEMENTARY NOTES

None

12a. DISTRIBUTION/AVAILABILITY STATEMENT

Approved for public release; distribution is unlimited.

12b. DISTRIBUTION CODE

13. ABSTRACT (*Maximum 200 words*)

The feasibility of acquiring satellites from the ground by using infrared focal-plane-array detectors is analyzed. The orbits of the satellites are assumed to be known to within a position uncertainty of ±50 km. Effects of the atmosphere have been modeled by the LOWTRAN7 code. Properties of five different available detectors have been inserted in the mathematical model. A telescope aperture of 60 cm (≈24 inches) is assumed in the numerical evaluations. Results are presented in graphs showing the region of space within which each candidate detector array can sense a satellite of a given infrared signature. The PtSi array can sense a medium-sized satellite in low earth orbit. A small, low-orbit satellite can be sensed at a low elevation by the HgCdTe array. That same array could also sense a medium-sized satellite at a 10,000-km altitude. Results for the InSb, Si:Ga, and IrSi arrays fall between these extremes.

14. SUBJECT TERMS	15. NUMBER OF PAGES
tbd	60
	16. PRICE CODE

17. SECURITY CLASSIFICATION OF REPORT	18. SECURITY CLASSIFICATION OF THIS PAGE	19. SECURITY CLASSIFICATION OF ABSTRACT	20. LIMITATION OF ABSTRACT
Unclassified	Unclassified	Unclassified	SAR

SUPPLEMENTARY

INFORMATION

ERRATUM

Document: Technical Report 919, "Performance of Ground-Based Infrared Detectors for Acquisition of Satellites"

Equation (7) on page 21 currently reads

$$S = \frac{A_T \tau_O Q t_{INT}}{4\pi R^2} \qquad (7)$$

It should read

$$S = \frac{A_T \tau_O Q t_{INT}}{R^2} \qquad (7)$$

None of the numerical calculations in the report were affected by the misstatement of Equation (7).

8 July 1992

Publications Office
MIT Lincoln Laboratory
PO Box 73
Lexington, MA 02173-9108

ERRATUM

Document: Technical Report 919, "Performance of Ground-Based Infrared Detectors for Acquisition of Satellites"

Equation (7) on page 21 currently reads

$$S = \frac{A_T \tau_O Q t_{INT}}{4\pi R^2} \qquad (7)$$

It should read

$$S = \frac{A_T \tau_O Q t_{INT}}{R^2} \qquad (7)$$

None of the numerical calculations in the report were affected by the misstatement of Equation (7).

8 July 1992

Publications Office
MIT Lincoln Laboratory
PO Box 73
Lexington, MA 02173-9108